

Efficient time splitting schemes for the monodomain equation in cardiac electrophysiology

Laura P. Lindner¹ | Tobias Gerach² | Tobias Jahnke¹  | Axel Loewe²  | Daniel Weiss¹ | Christian Wieners¹ 

¹Institute of Applied and Numerical Mathematics, Karlsruhe Institute of Technology (KIT), Karlsruhe, Germany

²Institute of Biomedical Engineering, Karlsruhe Institute of Technology (KIT), Karlsruhe, Germany

Correspondence

Christian Wieners, Institute of Applied and Numerical Mathematics, Karlsruhe Institute of Technology (KIT), Karlsruhe, Germany.

Email: christian.wieners@kit.edu

Funding information

Deutsche Forschungsgemeinschaft (DFG, German Research Foundation), Grant/Award Numbers: SPP 2311, 465189069, SFB 1173, 258734477; Ministry of Science, Research and the Arts Baden-Württemberg; Federal Ministry of Education and Research

Abstract

Approximating the fast dynamics of depolarization waves in the human heart described by the monodomain model is numerically challenging. Splitting methods for the PDE-ODE coupling enable the computation with very fine space and time discretizations. Here, we compare different splitting approaches regarding convergence, accuracy, and efficiency. Simulations were performed for a benchmark problem with the Beeler–Reuter cell model on a truncated ellipsoid approximating the left ventricle including a localized stimulation. For this configuration, we provide a reference solution for the transmembrane potential. We found a semi-implicit approach with state variable interpolation to be the most efficient scheme. The results are transferred to a more physiological setup using a bi-ventricular domain with a complex external stimulation pattern to evaluate the accuracy of the activation time for different resolutions in space and time.

KEYWORDS

Beeler–Reuter cell model, cardiac electrophysiology, monodomain equation, splitting methods, time integration

1 | INTRODUCTION

To replicate the human heart's function numerically, the efficient approximation of the electrophysiology plays a key role, since the overall cardiac mechanisms are controlled by the propagation of the depolarization waves and the chemical reactions, which are initiated by the electric stimulus. This process is described by the physiology-based bidomain equations consisting of two partial differential equations (PDEs) for modeling the intra- and extracellular potentials. The PDEs are coupled with a system of ordinary differential equations (ODEs) for the cellular model describing the ion currents across the membrane. A detailed derivation of the bidomain model is given by Franzoni and Savaré.¹ Under the assumption that the anisotropic intra- and extracellular conductivities are proportional to each other, the bidomain model can be reduced to the monodomain model. This model is simpler because it involves only one parabolic PDE describing the transmembrane voltage v , that is, the difference of the intra- and extracellular potentials. The monodomain model is computationally less demanding but still reproduces the main phenomena of wave propagation in the heart, see, for example, Bourgault and Pierre.²

This is an open access article under the terms of the [Creative Commons Attribution-NonCommercial-NoDerivs](https://creativecommons.org/licenses/by-nc-nd/4.0/) License, which permits use and distribution in any medium, provided the original work is properly cited, the use is non-commercial and no modifications or adaptations are made.

© 2022 The Authors. *International Journal for Numerical Methods in Biomedical Engineering* published by John Wiley & Sons Ltd.

A major computational challenge for the monodomain model is the large range of time scales varying from about a second for the heart beat to dozens of transitions per milliseconds for the fast gates of the ion channels. Since for realistic cell models a fully implicit scheme in time is prohibitively expensive due to the large number of unknowns, the standard approach is to use a splitting method for the time integration of the coupled PDE-ODE system. This means that in each time step, the ODEs describing the gating mechanisms, the ODEs for the evolution of the intracellular ion concentrations and the parabolic PDE for the transmembrane voltage are propagated successively. We denote this approach as component-wise splitting. Commonly, an additional operator splitting of the PDE into the reaction and the diffusion part is used. Schemes based on the reaction–diffusion splitting are for example the first-order Godunov method³ or the second-order Strang splitting.⁴ Because of the very fast dynamics of the gating mechanisms, the operator splitting approach is often combined with the observation of Rush and Larsen⁵ that the (linear) ODEs describing the gating variables can be solved exactly as long as the transmembrane voltage is kept fixed. This idea can also be used in the component-wise splitting approach.

As there is no analytical solution of the monodomain problem, the accuracy of time integration approaches has to be studied numerically. Niederer et al.⁶ defined a benchmark problem on a 3d cuboid and studied the approximations of the activation time on 11 different simulation codes for cardiac simulations. However, no systematic comparison of different numerical schemes was performed. Sundnes et al.³ confirmed the convergence behavior of several operator splitting methods combined with the simple FitzHugh–Nagumo model for a 1d domain. We extend these results to more complex membrane models and geometrical domains. The dependency of the conduction velocity on the spatial resolution was reported in several studies.^{7,8} We study the effect of both space and time discretization on this phenomenon in an unstructured anatomically motivated mesh. More recently, the convergence and accuracy of time integrators were studied on 1d and 2d regular rectangular domains with simplified external stimuli, for example by Roy et al.⁹ and Woodworth et al.¹⁰ However, as Krishnamoorthi et al.¹¹ already observed, the irregularity of the mesh has an immense impact on physiological properties and will thus be considered in the present study. As realistic heart simulations are performed on non-uniform meshes, it is essential to test the behavior of commonly used time integration approaches systematically for more complex and anatomically more relevant scenarios.

Here, we define a new anatomically more realistic and numerically more challenging electrophysiology benchmark problem on a truncated ellipsoid approximating the left ventricle, similar to the elasticity benchmark of Land et al.¹² For this more realistic configuration, we investigate splitting schemes in time systematically by comparing different approaches in terms of stability and accuracy. The latter is done by means of a reference solution computed on a very fine mesh and with a very small time step. Furthermore, we evaluate computational efficiency. This extends results for the Godunov splitting as well as implicit methods discretizing the parabolic PDE for the transmembrane voltage.^{13,14}

For the numerical computation, we use the parallel finite element system M++,¹⁵ which allows for very fine resolutions in space and time in order to obtain a reliable reference solution; this is required for the evaluation of the accuracy of the different time stepping schemes.

This work is a first comprehensive comparison of splitting approaches for the cardiac monodomain model regarding convergence in time and space, accuracy and efficiency. The test problems are anatomically more realistic and numerically more challenging than in previous works.

Nonlinear coupled PDE-ODE systems arise in many other physical applications, for example, porous-media modeling coupled to chemical processes or fractional diffusion realized with memory variables. But then a corresponding comparison of splitting approaches may yield different results, since the efficiency of the methods strongly depend on the application parameters, the nonlinearity, and the stiffness of the ODE components.

The paper is organized as follows: First, we introduce the monodomain equation and the Beeler–Reuter model, which we use in our investigation in detail. Different numerical approximation schemes of the coupled PDE-ODE system in space and in time are described in the third section. In Section 4, we define a benchmark problem on a truncated ellipsoid, provide a reference solution and study the convergence behavior and accuracy of different splitting approaches. In addition, we extend the investigation to a more realistic bi-ventricular domain. Finally, we conclude with a summary and an outlook on possible extensions of our results.

2 | THE MONODOMAIN EQUATION IN ELECTROPHYSIOLOGY

Modeling the electrophysiology in the human heart by the bidomain equation comprises the evolution of the extracellular and intra-cellular electric potentials, the concentration of several ions as well as the switching of gating

variables which control the transport of ions across the membranes, compare, Vigmond et al.¹⁶ In our convergence study of time integration schemes, we consider a model, which combines the monodomain equation for the transmembrane voltage (the difference of the extra-cellular and intra-cellular electric potentials) with a representative cell model introduced by Beeler and Reuter.¹⁷

Let $\Omega \subset \mathbb{R}^3$ be a bounded Lipschitz domain and let $[0, T]$ be a time interval. The model describes the evolution of the transmembrane voltage v , the intra-cellular calcium ion concentration c , and the vector of six gating variables \mathbf{w} , solving the coupled PDE-ODE system

$$\chi C_m \partial_t v - \nabla \cdot (\mathbf{D} \nabla v) + \chi I_{\text{ion}}(v, c, \mathbf{w}) = \chi I_{\text{ext}}, \quad (1a)$$

$$\partial_t c - G_c(v, c, \mathbf{w}) = 0, \quad (1b)$$

$$\partial_t \mathbf{w} - \mathbf{G}_w(v, \mathbf{w}) = \mathbf{0} \quad (1c)$$

in $[0, T] \times \Omega$ subject to the initial values at $t = 0$

$$v(0, \mathbf{x}) = v^0(\mathbf{x}), \quad c(0, \mathbf{x}) = c^0(\mathbf{x}), \quad \mathbf{w}(0, \mathbf{x}) = \mathbf{w}^0(\mathbf{x}), \quad \mathbf{x} \in \overline{\Omega} = \Omega \cup \partial\Omega \quad (1d)$$

and homogeneous Neumann boundary conditions

$$\mathbf{D} \nabla v \cdot \mathbf{n} = 0 \quad \text{on } (0, T) \times \partial\Omega. \quad (1e)$$

Parameters of the monodomain model are the surface-to-volume ratio $\chi \in \mathbb{R}_+$, the membrane capacitance $C_m \in \mathbb{R}_+$, and the conductivity tensor $\mathbf{D} : \overline{\Omega} \rightarrow \mathbb{R}^{3 \times 3}$ depending on the anisotropic cell structure, where we assume that the conductivity tensor \mathbf{D} is symmetric, bounded and uniformly positive definite. For the Beeler–Reuter cell model, the total ionic current in (1a) is of the form

$$I_{\text{ion}}(v, c, \mathbf{w}) = I_s(v, c, w_1, w_2) + I_{\text{Na}}(v, w_3, w_4, w_5) + I_{x_1}(v, w_6) + I_K(v), \quad (2)$$

depending polynomially on the gating variables \mathbf{w} , continuously on the electric voltage v , and logarithmically on the concentration c . The evolution is driven by the pacing from the cardiac conduction system comprising among other the sinus node in the atria and the Purkinje fibers in the ventricles. This is modeled by an external stimulus

$$I_{\text{ext}} : [0, T] \times \overline{\Omega} \rightarrow \mathbb{R}, \quad I_{\text{ext}}(t, \mathbf{x}) = \begin{cases} a_i(t, \mathbf{x}) & \text{for } t \in [t_{\text{beg},i}, t_{\text{beg},i} + \tau_i], \mathbf{x} \in \overline{\Omega}_{\text{stim},i}, \\ 0 & \text{else} \end{cases} \quad (3)$$

in the stimulation area $\overline{\Omega}_{\text{stim}} = \bigcup_{i=1, \dots, n_{\text{stim}}} \overline{\Omega}_{\text{stim},i} \subset \overline{\Omega}$. Here, $\Omega_{\text{stim},i}$ are disjoint sets, a_i are amplitude functions, $t_{\text{beg},i} \in [0, T - \tau_i]$ is the starting time of the i -th stimulus and $\tau_i > 0$ is its duration ($i = 1, \dots, n_{\text{stim}}$). In many applications the amplitude functions of the external stimulus I_{ext} are chosen to be constant functions, that is, $a_i(t, \mathbf{x}) = a_i > 0$ in (3); compare 8,10,14. In this case, however, the function I_{ext} is discontinuous both in time and space, and the missing regularity has the effect that convergence of the numerical methods can only be observed for very fine discretizations. This is not appropriate for the numerical convergence study of the different time stepping schemes in Section 4. In our simulations, therefore, we use amplitudes for the external current I_{ext} of the form $a_i(t, \mathbf{x}) = a_{t,i}(t) a_{\mathbf{x},i}(\mathbf{x}) a_i$, $i = 1, \dots, n_{\text{stim}}$, with $a_i > 0$ and

$$a_{t,i}(t) = \frac{1}{\pi} \left(\arctan(s_{\text{ext}}(t - t_{\text{beg},i})) - \arctan(s_{\text{ext}}(t - (t_{\text{beg},i} + \tau_i))) \right), \quad a_{\mathbf{x},i}(\mathbf{x}) = 1 - \min \left\{ 1, \frac{\text{dist}(\mathbf{x}, \overline{\Omega}_{\text{stim},i})}{l_{\text{exc}}} \right\}, \quad (4)$$

where $s_{\text{ext}} \in \mathbb{R}$ is a constant scaling factor and where the stimulus area is extended by $\Omega_{\text{stim},i} \subset \Omega_{\text{exc},i} \subset \overline{\Omega}$ in all directions approximately by the length l_{exc} (see Figure B1 in the Appendix). With this choice, the external stimulus I_{ext} defined in (3) is smooth in time and both continuous and weakly differentiable in space. Alternatively, for simulations of a single

heartbeat, the external stimulus can be replaced by suitable initial data v^0 of the transmembrane voltage, see, for example references 3,13.

The gating mechanisms at the membrane are described by the dimensionless vector $\mathbf{w} = (w_1, \dots, w_6)$. Depending on non-negative opening and closing rates $\alpha_k(v)$ and $\beta_k(v)$, the evolution is determined by

$$\mathbf{G}_{\mathbf{w}}(v, \mathbf{w}) = (G_k(v, w_k))_{k=1, \dots, 6} \quad \text{with} \quad G_k(v, w_k) = \alpha_k(v) - (\alpha_k(v) + \beta_k(v))w_k, \quad k = 1, \dots, 6. \quad (5)$$

Starting with $w_k(0, \mathbf{x}) \in [0, 1]$, we obtain $w_k(t, \mathbf{x}) \in [0, 1]$ by construction from $G_k(v, 0) \geq 0$ and $G_k(v, 1) \leq 0$.

The evolution of the calcium concentration depends on the ionic current I_s and is of the form

$$G_c(v, c, \mathbf{w}) = -\alpha_c I_s(v, c, w_1, w_2) + w_c(\alpha_c - c). \quad (6)$$

All parameters, the explicit equations for the ionic currents, and the opening and closing rates for the Beeler–Reuter model are summarized in the Appendix A. For the extension to more complex ionic models, the corresponding function G_c has to be adapted, see, for example, (18, Supplement) for the O'Hara and Rudy model.

3 | NUMERICAL APPROXIMATION OF THE MONODOMAIN EQUATION

The PDE-ODE system (1) is discretized in space by conforming finite elements for the voltage v and nodal values for (c, \mathbf{w}) . For the time discretization we discuss and compare different splitting methods. All methods described in Section 3.2 are based on the component-wise splitting. The difference is the way how the PDE for the transmembrane voltage is treated.

3.1 | Discretization in space

Let $\Omega_h = \cup_{K \in \mathcal{K}_h} K$ be a decomposition into open tetrahedra, and let $V_h = \{\phi_h \in C^0(\overline{\Omega}) : \phi_h|_K \in \mathbb{P}_1(K) \text{ for all } K \in \mathcal{K}_h\}$ be the approximation space of lowest order conforming finite elements. All functions $\phi_h \in V_h$ are uniquely defined by their nodal values $(\phi_h(\mathbf{x}))_{\mathbf{x} \in \mathcal{N}_h}$ at the corner points $\mathcal{N}_h \subset \overline{\Omega}$ of the triangulation. Let $\Pi_h : C^0(\overline{\Omega}) \rightarrow V_h$ be the corresponding nodal interpolation defined by $\Pi_h(\phi)(\mathbf{x}) = \phi(\mathbf{x})$ for $\mathbf{x} \in \mathcal{N}_h$. Let V'_h be the dual space of V_h , and let $\langle \cdot, \cdot \rangle$ denote the dual pairing.

We define $M_h, A_h \in \mathcal{L}(V_h, V'_h)$ by

$$\langle M_h \phi_h, \psi_h \rangle = \int_{\Omega} \phi_h \psi_h \, d\mathbf{x}, \quad \langle A_h \phi_h, \psi_h \rangle = \chi^{-1} \int_{\Omega} (\mathbf{D} \nabla \phi_h) \cdot \nabla \psi_h \, d\mathbf{x}, \quad \phi_h, \psi_h \in V_h.$$

The discrete operators M_h and A_h are represented as (parallel distributed) matrices and are assembled only once. The extension of the operator M_h to $M \in \mathcal{L}(L_2(\Omega), V'_h)$ defined by

$$\langle M \phi, \psi_h \rangle = \int_{\Omega} \phi \psi_h \, d\mathbf{x}, \quad \phi \in L_2(\Omega), \psi_h \in V_h$$

can be realized only approximately. For continuous functions ϕ , $M\phi$ can be approximated by $M_h \Pi_h \phi$. Alternatively, it can be approximated by the numerical integration operator $\mathcal{M}_h \in \mathcal{L}(C^0(\overline{\Omega}), V'_h)$ defined by a quadrature rule

$$\langle \mathcal{M}_h \phi, \psi_h \rangle = \sum_{K \in \mathcal{K}_h} \sum_{q=1}^{n_{\text{quad}}} \omega_{K,q} \phi(\mathbf{x}_{K,q}) \psi_h(\mathbf{x}_{K,q}), \quad \phi \in C^0(\overline{\Omega}), \psi_h \in V_h$$

with weights $\omega_{K,q} > 0$ and integration points $\mathbf{x}_{K,q} \in K$ for $q = 1, \dots, n_{\text{quad}}$, so that $\mathcal{M}_h \phi_h = M_h \phi_h$ for $\phi_h \in V_h$. We will show in our evaluation of different schemes that using numerical quadrature $\mathcal{M}_h \phi_h$ instead of interpolation $M_h \Pi_h \phi$ improves the stability in case that ϕ is not smooth enough. In the terminology introduced by Pathmanathan et al.¹⁹ the

evaluation by the approximative L_2 integral corresponds to the state variable interpolation (SVI), and the Lagrange interpolation is the ionic current interpolation (ICI).

The semi-discrete equation in space determines $(v_h, c_h, \mathbf{w}_h) : [0, T] \rightarrow V_h^8$ by

$$C_m M_h \partial_t v_h + A_h v_h + \mathcal{M}_h I_{\text{ion}}(v_h, c_h, \mathbf{w}_h) = \mathcal{M}_h I_{\text{ext}} \quad \text{in } V_h', \quad (7a)$$

$$\partial_t c_h - G_c(v_h, c_h, \mathbf{w}_h) = 0 \quad \text{for all } \mathbf{x} \in \mathcal{N}_h, \quad (7b)$$

$$\partial_t \mathbf{w}_h - \mathbf{G}_w(v_h, \mathbf{w}_h) = \mathbf{0} \quad \text{for all } \mathbf{x} \in \mathcal{N}_h \quad (7c)$$

subject to the initial values at $t = 0$

$$v_h(0, \mathbf{x}) = v^0(\mathbf{x}), \quad c_h(0, \mathbf{x}) = c^0(\mathbf{x}), \quad \mathbf{w}_h(0, \mathbf{x}) = \mathbf{w}^0(\mathbf{x}), \quad \mathbf{x} \in \mathcal{N}_h \quad (7d)$$

obtained by nodal interpolation of (1d), where we assume that the initial data (v^0, c^0, \mathbf{w}^0) are continuous. For the numerical experiments in Section 4 the initial conditions are constant in space. Note, that for the ODE evolution in (7b) and (7c) the evaluation at the nodal points \mathcal{N}_h is sufficient, but in general the application of \mathcal{M}_h in (7a) requires the evaluation of (c_h, \mathbf{w}_h) at the integration points in every cell $K \in \mathcal{K}_h$.

3.2 | Discretization in time

Let $N \in \mathbb{N}$ be the number of time steps, let $\Delta t = T/N$ be the step-size of the time discretization, and set $t_n = n\Delta t$. Starting with $(v_h^0, c_h^0, \mathbf{w}_h^0)$ given by (7d), we now present different methods for computing the next iterate $(v_h^n, c_h^n, \mathbf{w}_h^n)$ from the approximations $(v_h^{n-1}, c_h^{n-1}, \mathbf{w}_h^{n-1})$ in the previous time step.

It is well-known that the space discretization of the PDE (1a) leads to a stiff ODE system. If an explicit Runge–Kutta or multi-step method is applied to this ODE, then an extremely small step-size has to be used in order to ensure stability. Such a severe step-size restriction can be avoided by using an A -stable or $A(\alpha)$ -stable time integrator instead, but such methods are implicit. This means that in every time step a nonlinear system of equations has to be solved. Applying such a method to the *full* system (1) is thus computationally very expensive. Another numerical challenge is the fast switching of the gating variables. If the solution of (1c) is approximated, say, with a Runge–Kutta method, then again a very small step-size has to be chosen to obtain an acceptable accuracy.

For these reasons the component-wise splitting is very popular and widely used.^{13,14} In this approach every time step for propagating the system (7) consists of three sub-steps. In each of these sub-steps, only *some* of the unknowns are updated, while the others are kept fixed: first, the gating variables are updated, then the calcium concentration, and finally the transmembrane voltage. Interchanging the order of these three sub-steps is possible and yields a different but similar method with nearly the same accuracy.

3.2.1 | Exact propagation of the gating variables

For fixed transmembrane voltage v_h^{n-1} the ODE (1c) for the gating variables is linear in \mathbf{w} and decoupled in all components (see (5)). In (7c) the ODE for given $(v_h^{n-1}, \mathbf{w}_h^{n-1})$ takes the form

$$\partial_t w_{h,k} = \alpha_k(v_h^{n-1}) - (\alpha_k(v_h^{n-1}) + \beta_k(v_h^{n-1}))w_{h,k} \quad \text{for } t \in (t_{n-1}, t_n) \quad \text{with } w_{h,k}(t_{n-1}) = w_{h,k}^{n-1}, k = 1, \dots, 6.$$

As suggested by Rush and Larsen,⁵ this ODE can be solved exactly, so that we get $w_{h,k}(t_n) = \varphi_k^{\Delta t}(v_h^{n-1}, w_{h,k}^{n-1})$ with

$$\varphi_k^{\Delta t}(v_h, w_{h,k}) = w_{k,\infty}(v_h) + (w_{h,k} - w_{k,\infty}(v_h)) \exp(-\Delta t(\alpha_k(v_h) + \beta_k(v_h))), \quad w_{k,\infty}(v) = \frac{\alpha_k(v)}{\alpha_k(v) + \beta_k(v)}. \quad (8)$$

This defines $\mathbf{w}_h^n = \boldsymbol{\varphi}^{\Delta t}(v_h^{n-1}, \mathbf{w}_h^{n-1})$ with $\boldsymbol{\varphi}^{\Delta t} = (\varphi_k^{\Delta t})_{k=1, \dots, 6}$.

3.2.2 | Explicit Euler method for the calcium concentration

The ODE (7b) for the calcium concentration is not stiff. Hence, for given $(v_h^{n-1}, c_h^{n-1}, \mathbf{w}_h^n)$, we can simply update c_h^{n-1} with one step of the explicit Euler method

$$c_h^n = c_h^{n-1} + \Delta t G_c(v_h^{n-1}, c_h^{n-1}, \mathbf{w}_h^n). \quad (9)$$

Combining the exact solution (8) with the explicit Euler approximation (9) plus an explicit Euler approximation of the nonlinear part of (10) is called *Rush-Larsen method*; compare, references 5,20,21.

3.2.3 | Time stepping for the transmembrane voltage

In the third sub-step the solution of the semi-linear parabolic equation

$$C_m M_h \partial_t v_h + A_h v_h + F(t, v_h, c_h^n, \mathbf{w}_h^n) = 0 \quad \text{for } t \in (t_{n-1}, t_n) \quad \text{with } v_h(t_{n-1}) = v_h^{n-1} \quad (10)$$

with $F(t, v_h, c_h, \mathbf{w}_h) = \mathcal{M}_h(I_{\text{ion}}(v_h, c_h, \mathbf{w}_h) - I_{\text{ext}}(t, \cdot))$ has to be approximated for given $(v_h^{n-1}, c_h^n, \mathbf{w}_h^n)$.

We compare several options:

(GS) A standard approach for the monodomain problem is the Godunov splitting: with $\partial_t v_h \approx (\Delta t)^{-1}(v_h^n - v_h^{n-1})$ and $F(t, v_h, c_h, \mathbf{w}_h) \approx M_h \Pi_h(I_{\text{ion}}(v_h, c_h, \mathbf{w}_h) - I_{\text{ext}}(t, \cdot))$, we can introduce an intermediate update $v_h^{n-1/2}$ and define

$$v_h^{n-1/2} = v_h^{n-1} - \Delta t C_m^{-1} (I_{\text{ion}}(v_h^{n-1}, c_h^n, \mathbf{w}_h^n) - I_{\text{ext}}(t_n, \cdot)), \quad (11a)$$

$$(C_m M_h + \Delta t A_h) v_h^n = C_m M_h v_h^{n-1/2}. \quad (11b)$$

This corresponds to one step of the Godunov splitting (which is rather called Lie–Trotter splitting in numerical analysis) applied to (10). In this form it is realized, for example, in openCARP.²² For our tests we improve the approximation of the external current I_{ext} by numerical integration, that is,

$$v_h^{n-1/2} = v_h^{n-1} - \Delta t C_m^{-1} I_{\text{ion}}(v_h^{n-1}, c_h^n, \mathbf{w}_h^n), \quad (12a)$$

$$(C_m M_h + \Delta t A_h) v_h^n = C_m M_h v_h^{n-1/2} + \Delta t \mathcal{M}_h I_{\text{ext}}(t_n, \cdot). \quad (12b)$$

In comparison with other splitting schemes, we use (12) to exclude the error from the difference $(M_h \Pi_h - \mathcal{M}_h) I_{\text{ext}}$ in the evaluation of the external current.

As an alternative to (GS) the following implicit methods are considered:

(IE-SVI) The implicit Euler method computes the approximation v_h^n by solving the nonlinear equation

$$(C_m M_h + \Delta t A_h) v_h^n - C_m M_h v_h^{n-1} + \Delta t F(t_n, v_h^n, c_h^n, \mathbf{w}_h^n) = 0 \quad (13)$$

with several Newton steps.

(LI-SVI) If only one single Newton step is used, then this yields the linearly implicit scheme

$$(C_m M_h + \Delta t A_h + \Delta t \partial_v F(t_n, v_h^{n-1}, c_h^n, \mathbf{w}_h^n)) v_h^n = C_m M_h v_h^{n-1} + \Delta t (\partial_v F(t_n, v_h^{n-1}, c_h^n, \mathbf{w}_h^n) v_h^{n-1} - F(t_n, v_h^{n-1}, c_h^n, \mathbf{w}_h^n)) \quad (14)$$

with $\partial_v F(t_n, v_h, c_h, \mathbf{w}_h) = \mathcal{M}_h \partial_v I_{\text{ion}}(v_h, c_h, \mathbf{w}_h)$.

(SI-SVI) If only the linear part of (10) is treated with the implicit Euler method, whereas the nonlinear part is updated with the explicit Euler method, then this leads to the semi-implicit method

$$(C_m M_h + \Delta t A_h) v_h^n = C_m M_h v_h^{n-1} - \Delta t F(t_n, v_h^{n-1}, c_h^n, \mathbf{w}_h^n). \quad (15)$$

The SI-SVI differs from (12) only in evaluation of total ionic current, where $M_h \Pi_h I_{\text{ion}}(v_h, c_h, \mathbf{w}_h)$ is replaced by $\mathcal{M}_h I_{\text{ion}}(v_h, c_h, \mathbf{w}_h)$.

The finite element matrix $C_m M_h + \Delta t A_h$ is identical for all time steps and has to be assembled only once if the Godunov splitting (GS) or the semi-implicit method (SI-SVI) are used in the third sub-step (3). For the linearly implicit scheme (LI-SVI) we have to assemble and add the derivative of F in every time step. The implicit Euler method (IE-SVI) is even more demanding, because here this has to be done in each iteration of Newton's method. For the SVI method, the right-hand side $F(t, v_h, c_h, \mathbf{w}_h) = \mathcal{M}_h (I_{\text{ion}}(v_h, c_h, \mathbf{w}_h) - I_{\text{ext}}(t, \cdot))$ has to be assembled in every time step. This can be simplified by the approximation $F(t, v_h, c_h, \mathbf{w}_h) \approx M_h \Pi_h (I_{\text{ion}}(v_h, c_h, \mathbf{w}_h) - I_{\text{ext}}(t, \cdot))$ using nodal interpolation (ICI) and then multiplication with the sparse mass matrix M_h ; this is realized by the Godunov splitting (11).

The ODEs (7b) and (7c) are solved in parallel at all nodal points $\mathbf{x} \in \mathcal{N}_h$. The only global interaction is the solution of the PDE (7a) in every time step. In case of the Godunov splitting, (12a) is solved in parallel for all nodal points and only for the diffusion part (12b) a global interaction is present.

In the component-wise splitting described above, the three sub-problems (1), (2), (3) are propagated one after another with the same step-size Δt . This yields a first-order method, that is, the global error of the time integration is $\mathcal{O}(\Delta t)$ under certain regularity assumptions on the exact solution. A second-order method with error $\mathcal{O}(\Delta t^2)$ could, in principle, be obtained if the three sub-steps were arranged in a symmetric way, and if the numerical schemes in each of the sub-steps were replaced by second-order schemes. However, each time step of a second-order method is more costly than a step with a first-order method. Typically, one expects that the higher costs per time step are compensated by a higher accuracy, such that a much larger step-size and thus a smaller number of time steps can be chosen. However, this is only true if the problem is sufficiently regular, and such a degree of regularity cannot be expected for the problem (1). This is the reason why we consider only first-order time integration in this work. Since the component-wise splitting is a first-order method, it does not give much of an improvement to replace the explicit Euler method in step (2) by a higher-order Runge–Kutta method; this is confirmed by numerical tests (this can be reproduced with our code in the git repository²³ by changing the calcium update in the staggered scheme). On the other hand, higher order time stepping schemes for the ODE system are successfully applied to cardiac electrophysiology²⁴ without PDE coupling.

4 | NUMERICAL EVALUATION OF TIME-STEPPING SCHEMES

In our numerical investigations, we propose, in a first step, a benchmark configuration in form of a truncated ellipsoid, where the excitation is initiated at the bottom by an external current, which is smooth in space and time. The accuracy and efficiency of the different schemes are measured by the evolution of the transmembrane voltage at several test points. In a second step, we perform a convergence test in space and time by evaluating the activation time on a realistic bi-ventricular domain. This requires to include a physiological stimulation model representing the effect of the His-Purkinje system.

We start with a precise definition of the test configuration. Then, we provide a reference solution, which is used for the evaluation of the different approaches. Finally, we test numerically the convergence in space and time of the activation time for a full bi-ventricular geometry.

4.1 | A benchmark configuration for the monodomain model

In the computational domain Ω we prescribe fiber directions $\mathbf{f} : \Omega \rightarrow \mathbb{R}^3$ which define the conductivity tensor in (1a)

$$\mathbf{D}(\mathbf{x}) = D_1 \mathbf{f}(\mathbf{x}) \otimes \mathbf{f}(\mathbf{x}) + D_t \left(\mathbf{I} - \mathbf{f}(\mathbf{x}) \otimes \mathbf{f}(\mathbf{x}) \right) \in \mathbb{R}_{\text{sym}}^{3 \times 3}, \quad \mathbf{x} \in \bar{\Omega}, \quad (16)$$

depending on the conductivities D_l and D_t in longitudinal and transversal direction (see Appendix B.1 for all parameters and mesh data). To avoid a reduction of the regularity, we use only the space and time continuous version of I_{ext} defined in (4) in our simulations.

For the convergence tests, we consider the transmembrane voltage $v(t, \mathbf{z}_k)$ in $(0, T)$ at selected points $\mathbf{z}_k \in \bar{\Omega}$. Furthermore, we determine the activation time at these points \mathbf{z}_k , which is a frequently used quantity in the comparison of different cell models. In our benchmark scenario, we use an ellipsoid approximating the human ventricle, where the geometry is truncated and the final time $T = 30$ ms is chosen so that all evaluation points are activated in $(0, T)$. The evaluation points \mathbf{z}_k for the truncated ellipsoid are illustrated in Figure 1 (yellow dots) as well as the stimulus area Ω_{exc} for the discrete external current on the coarse grid. In this test, we use only one stimulation area, that is, $n_{\text{stim}} = 1$. The position of the evaluation points \mathbf{z}_k are described in detail in Table B1.

As a first test geometry, we used an idealized left ventricle based on the truncated ellipsoid defined in reference 12 with a fiber orientation ranging from -60° at the epicardial surface to $+60^\circ$ at the endocardial surface. Furthermore, the geometry was truncated closer to the apex to reduce the computational load and discretized with a tetrahedral mesh.

Let $h_0 > 0$ be the mesh size of the coarse mesh, and let Δt_0 be the largest time step-size. The convergence is investigated by refining in space with mesh size $h_\ell = 2^{-\ell} h_0$ on space level $\ell \in \mathbb{N}_0$ and in time with $\Delta t_j = 2^{-j} \Delta t_0$ on time level $j \in \mathbb{N}_0$, see Table 1, where we also include the mesh data for $\ell = 0, \dots, 6$. Note that the coarse mesh ($\ell = 0$) is only used to represent the geometry. At least three uniform mesh refinements are required for a sufficient approximation of the evolution of the system. The corresponding discrete solution is denoted by $v^{j,\ell}$. The distribution of the edge length Δx of the tetrahedral elements of the truncated ellipsoid is plotted for $\ell = 0$. For the higher levels, the distribution will be the same, only the absolute values of Δx is halved with every refinement.

All numerical experiments are performed on the high performance computing system HoreKa at KIT using the partition *cpuonly*. The problem is solved with the open source parallel finite element system M++.²³ The number of parallel processes was between 64 and 8192 depending on the problem size and memory requirements. The scalability of the

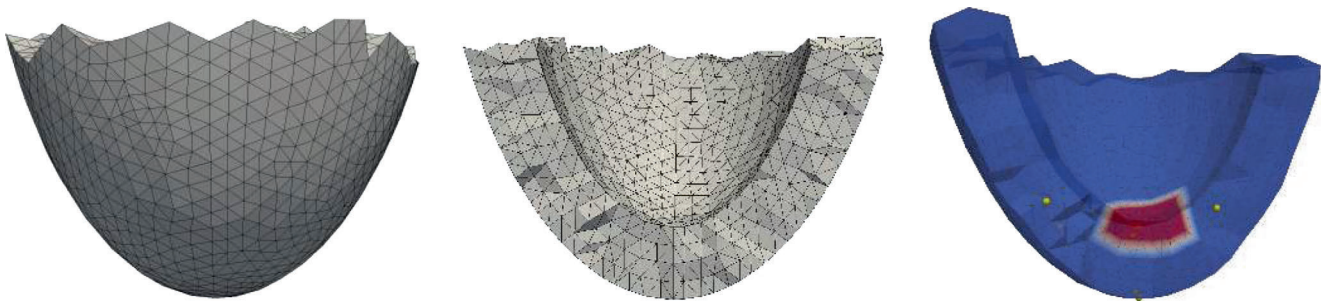


FIGURE 1 Geometry and coarse mesh on level $\ell = 0$ for the truncated ellipsoid (left and middle), activation area $\Omega_{\text{exc},1}$ and evaluation points \mathbf{z}_k (right).

TABLE 1 Mesh data for the space levels ℓ for the truncated ellipsoid configuration and time discretization on time levels j . Here, Δx is the length between two nodes of the mesh in mm. The figure on the right shows the relative frequency of different edge lengths in the mesh for $\ell = 0$.

| ℓ | min Δx | max Δx | # cells | # vertices | j | N_j | Δt_j (ms) |
|--------|----------------|----------------|---------------|-------------|-----|-------|-------------------|
| 0 | 0.22682 | 1.26099 | 18,136 | 3954 | 0 | 300 | 0.1 |
| 1 | 0.11341 | 0.63049 | 145,088 | 27,851 | 1 | 600 | 0.05 |
| 2 | 0.05670 | 0.31524 | 1,160,704 | 208,021 | 2 | 1200 | 0.025 |
| 3 | 0.02835 | 0.15762 | 9,285,632 | 1,605,673 | 3 | 2400 | 0.0125 |
| 4 | 0.01417 | 0.07881 | 74,285,056 | 12,612,689 | 4 | 4800 | 0.00625 |
| 5 | 0.00708 | 0.03940 | 594,280,448 | 99,973,281 | 5 | 9600 | 0.003125 |
| 6 | 0.00354 | 0.01970 | 4,754,243,584 | 796,078,401 | 6 | 19200 | 0.0015625 |

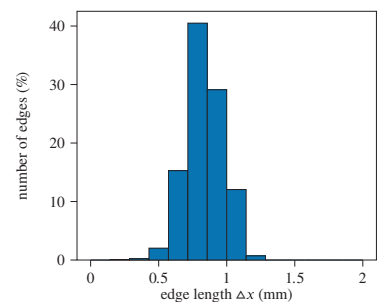


TABLE 2 CPU time for different number of processes for the semi-implicit (SI-SVI) approach, fixed space level $\ell = 3$ and fixed time level $j = 3$ with the benchmark configuration.

| Procs | 64 | 128 | 256 | 512 | 1024 |
|----------------------------------|---------|-------|-------|------|------|
| CPU time (hours:minutes:seconds) | 1:10:49 | 31:54 | 15:54 | 8:33 | 5:11 |

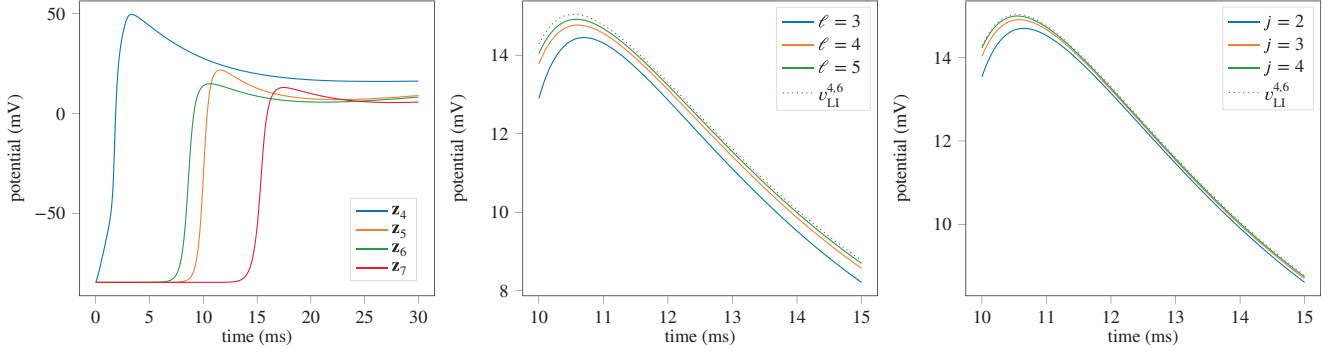


FIGURE 2 Evolution of the transmembrane voltage v at the different evaluation points $\mathbf{z}_k \in \Omega$ of our benchmark configuration (cf. Figure 1) computed with the LI-SVI, and convergence of the LI-SVI scheme to the reference solution in space with fixed $j = 3$ and in time with fixed $\ell = 5$ evaluated for $v_{LI}^{j,\ell}(t, \mathbf{z}_6)$, $t \in [10, 15]$ ms.

results regarding the CPU time is ensured, see, for example, Table 2 for a test with fixed levels in space and time, respectively.

4.2 | The reference solution

In the first step, we compute an asymptotic reference solution for the ellipsoidal configuration with different mesh sizes and time step-sizes. We investigate in detail LI-SVI and SI-SVI by comparing the approximations of the transmembrane voltage computed with very fine discretizations in space and time for both time integration methods. By extrapolation in space and time, we estimate the accuracy of the evolution of the transmembrane voltage at selected points.

In Figure 2, the evolution of the transmembrane voltage at $\mathbf{z}_4, \mathbf{z}_5, \mathbf{z}_6, \mathbf{z}_7 \in \Omega$ and the convergence in space and in time at \mathbf{z}_6 is shown for LI-SVI. The excitation wave arrives in the expected sequence depending on the fiber directions and the distances to the stimulus located in Ω_{stim} .

The computation of the error for the finest approximations of LI-SVI and SI-SVI is based on the estimate of the convergence order in space and time. From the differences of the solutions in space $v^{j,\ell}(\cdot, \mathbf{z}_k) - v^{j,\ell-1}(\cdot, \mathbf{z}_k)$ and in time $v^{j,\ell}(\cdot, \mathbf{z}_k) - v^{j-1,\ell}(\cdot, \mathbf{z}_k)$, compare, Table 3, the asymptotic convergence rate can be estimated from the factors $f_{j,\ell}$ and $g_{j,\ell}$ defined by

$$f_{j,\ell} = \frac{\|v^{j,\ell-1} - v^{j,\ell-2}\|_{L_2(0,T)}}{\|v^{j,\ell} - v^{j,\ell-1}\|_{L_2(0,T)}} \approx 2^{s_{\text{space}}}, \quad g_{j,\ell} = \frac{\|v^{j-1,\ell} - v^{j-2,\ell}\|_{L_2(0,T)}}{\|v^{j,\ell} - v^{j-1,\ell}\|_{L_2(0,T)}} \approx 2^{s_{\text{time}}}, \quad (17)$$

that is, $s_{\text{space}} \approx \log_2 f_{j,\ell}$ is the estimated convergence rate in space and $s_{\text{time}} \approx \log_2 g_{j,\ell}$ in time. Using extrapolation (see, e.g., ref. 25 Chapter 4.2.8), the limit approximations in space $v^{j,\infty}$ and time $v^{\infty,\ell}$ for $j = 0, \dots, J$ and $\ell = 0, \dots, L$ are computed from the finest computation on $\ell = L$ and $j = J$ by

$$v^{j,\infty} = \frac{f_{j,L}}{f_{j,L} - 1} v^{j,L} - \frac{1}{f_{j,L} - 1} v^{j,L-1}, \quad v^{\infty,\ell} = \frac{g_{J,\ell}}{g_{J,\ell} - 1} v^{J,\ell} - \frac{1}{g_{J,\ell} - 1} v^{J-1,\ell}. \quad (18)$$

TABLE 3 Convergence of $v^{j,\ell}$ in $\|\cdot\|_{L_2(0, T)}$ and convergence in space and in time (26) at the evaluation points \mathbf{z}_6 and \mathbf{z}_7 for the linearly implicit (LI-SVI) and the semi-implicit (SI-SVI) scheme

| $j=4$ | $\ell=4$ | $\ell=5$ | $\ell=6$ | $\ell=5$ | $\ell=6$ | $\ell=5$ | $j=3$ | $j=4$ | $j=5$ | $j=6$ |
|---|----------|----------|----------|---|----------|----------|--------|-------|-------|--------|
| $v_{LI}^{j,\ell}(\cdot, \mathbf{z}_6) - v_{LI}^{j,\ell-1}(\cdot, \mathbf{z}_6)$ | 0.1725 | 0.0523 | 0.0103 | $v_{LI}^{j,\ell}(\cdot, \mathbf{z}_6) - v_{LI}^{j-1,\ell}(\cdot, \mathbf{z}_6)$ | 0.1507 | 0.0658 | 0.0304 | | | |
| $\log_2 f_{j,\ell}$ | 1.72 | 2.34 | 1.19 | $\log_2 g_{j,\ell}$ | 1.11 | | | | | |
| $v_{LI}^{j,\ell}(\cdot, \mathbf{z}_7) - v_{LI}^{j,\ell-1}(\cdot, \mathbf{z}_7)$ | 0.5942 | 0.2099 | 0.0564 | $v_{LI}^{j,\ell}(\cdot, \mathbf{z}_7) - v_{LI}^{j-1,\ell}(\cdot, \mathbf{z}_7)$ | 0.2785 | 0.1231 | 0.0573 | | | |
| $\log_2 f_{j,\ell}$ | 1.50 | 1.89 | 1.17 | $\log_2 g_{j,\ell}$ | 1.10 | | | | | |
| $v_{SI}^{j,\ell}(\cdot, \mathbf{z}_6) - v_{SI}^{j,\ell-1}(\cdot, \mathbf{z}_6)$ | 0.1765 | 0.0538 | 0.0106 | $v_{SI}^{j,\ell}(\cdot, \mathbf{z}_6) - v_{SI}^{j-1,\ell}(\cdot, \mathbf{z}_6)$ | 0.0174 | 0.0126 | 0.0084 | | | 0.0048 |
| $\log_2 f_{j,\ell}$ | 1.71 | 2.34 | 0.46 | $\log_2 g_{j,\ell}$ | 0.58 | | | | | |
| $v_{SI}^{j,\ell}(\cdot, \mathbf{z}_7) - v_{SI}^{j,\ell-1}(\cdot, \mathbf{z}_7)$ | 0.6049 | 0.2144 | 0.0577 | $v_{SI}^{j,\ell}(\cdot, \mathbf{z}_7) - v_{SI}^{j-1,\ell}(\cdot, \mathbf{z}_7)$ | 0.0329 | 0.0092 | 0.0077 | | | 0.0048 |
| $\log_2 f_{j,\ell}$ | 1.49 | 1.89 | 1.83 | $\log_2 g_{j,\ell}$ | 0.25 | | | | | 0.68 |

TABLE 4 Estimates for the relative error for the reference solutions.

| | $\frac{\ v^{5,\infty}(\cdot, \mathbf{z}_k) - v^{\text{ref}}(\cdot, \mathbf{z}_k)\ _{L_2(0, T)}}{\ v^{5,\infty}(\cdot, \mathbf{z}_k)\ _{L_2(0, T)}}$ | $\frac{\ v^{\infty,5}(\cdot, \mathbf{z}_k) - v^{\text{ref}}(\cdot, \mathbf{z}_k)\ _{L_2(0, T)}}{\ v^{\infty,5}(\cdot, \mathbf{z}_k)\ _{L_2(0, T)}}$ | $\frac{\ v^{\infty,\infty}(\cdot, \mathbf{z}_k) - v^{\text{ref}}(\cdot, \mathbf{z}_k)\ _{L_2(0, T)}}{\ v^{\infty,\infty}(\cdot, \mathbf{z}_k)\ _{L_2(0, T)}}$ |
|---|---|---|---|
| $v_{\text{LI}}^{\text{ref}}(\cdot, \mathbf{z}_6)$ | 0.0055 | 0.0068 | 0.0089 |
| $v_{\text{LI}}^{\text{ref}}(\cdot, \mathbf{z}_7)$ | 0.0114 | 0.0050 | 0.0164 |
| $v_{\text{SI}}^{\text{ref}}(\cdot, \mathbf{z}_6)$ | 0.0018 | 0.0026 | 0.0013 |
| $v_{\text{SI}}^{\text{ref}}(\cdot, \mathbf{z}_7)$ | 0.0059 | 0.0070 | 0.0046 |

For both schemes, we observe quadratic convergence in space, compare, Table 3. For LI-SVI, we observe linear convergence in time. This is not as good for the SI-SVI scheme, where nearly linear convergence in time is observed only for sufficiently small time steps.

Quadratic convergence in space and linear convergence in time is now used to estimate the accuracy of the finest solutions by extrapolation first in space and in time, and then in both. This yields

$$v^{5,\infty} = \frac{4}{3}v^{5,5} - \frac{1}{3}v^{5,4}, \quad v^{\infty,5} = 2v^{5,5} - v^{4,5}, \quad v^{\infty,\infty} = 2v^{5,\infty} - v^{4,\infty}.$$

Now the reference solutions $v_{\text{LI}}^{\text{ref}} = v_{\text{LI}}^{4,6}$ and $v_{\text{SI}}^{\text{ref}} = v_{\text{SI}}^{5,6}$ are compared in Table 4 with the extrapolations.

We observe that the relative error estimated by extrapolation in space (left) and in time (middle) is nearly equilibrated, and extrapolating in space and time (right) shows that the relative error of $v_{\text{SI}}^{\text{ref}}$ is below 0.5% in both tests points. Since $v_{\text{LI}}^{\text{ref}}$ is computed with larger time steps, the estimated error is larger. However, the difference of the two solutions

$$\frac{\|v_{\text{LI}}^{\text{ref}}(\cdot, \mathbf{z}_6) - v_{\text{SI}}^{\text{ref}}(\cdot, \mathbf{z}_6)\|_{L_2(0, T)}}{\|v_{\text{LI}}^{\infty,\infty}(\cdot, \mathbf{z}_6)\|_{L_2(0, T)}} = 0.0089494$$

is below 1%, so that for both reference solutions the estimated error is of the same magnitude.

In summary, we observe that the errors in space and time for the linearly implicit scheme (LI-SVI) are balanced even for coarse space discretizations, and we can obtain the expected convergence orders in space and time. Nevertheless, the semi-implicit scheme (SI-SVI) is more accurate for the same discretizations, even if the space error is dominant and the time convergence cannot be observed for larger step-sizes.

4.3 | Comparison of different approximation schemes for the total ionic current

In general, we use the L_2 -projection (SVI) for the evaluation of (c_h^n, \mathbf{w}_h^n) in (7a). Since the ODEs in (7b) and (7c) are solved on the nodal points only, simply using Lagrange interpolation (ICI) in (7a) is numerically cheaper, but also less accurate as reported by Pathmanathan et al.¹⁹ for the semi-implicit case (SI). Here, this is confirmed for the linearly implicit scheme on our ellipsoidal benchmark configuration, compare, Table 5: the Lagrange interpolation takes $\approx 25\%$ less CPU time than the SVI approach. However, to achieve the same accuracy, one more space refinement is needed, which results in an approximately 12 times longer CPU time compared to the SVI on the lower level. In comparison with the reference solution the convergence of $v^{j,\ell}(\cdot, \mathbf{z}_6)$ to the reference solution in space and in time is monotone for SVI but not for ICI, where the error is smaller for $\ell = j$. This effect was also observed in reference 19 for different space discretizations. In summary, we conclude that the SVI approach is more efficient than ICI.

4.4 | Convergence of the conduction velocity

The spatial convergence behavior of the conduction velocity (CV) is investigated for the benchmark setup using the semi-implicit scheme (SI-SVI). The CV between two points $\mathbf{x}, \mathbf{y} \in \bar{\Omega}_{\text{act}}$ is defined by

TABLE 5 Accuracy of the transmembrane potential at \mathbf{z}_6 for the L_2 -projection (SVI) and the Lagrange interpolation (ICI) compared to v_{LI}^{ref} (left) and the required parallel CPU time (given in hours:minutes:seconds) (right) to solve the full system of the benchmark configuration with the linearly implicit scheme (LI).

| $\ \mathbf{v}^{j,\ell}(\cdot, \mathbf{z}_6) - \mathbf{v}_{LI}^{\text{ref}}(\cdot, \mathbf{z}_6) \ _{L_2(0, T)}$ | | SVI | | ICI | |
|--|---------|-------|----------|-------|----------|
| $\ell = 3$ | $j = 3$ | | 0.2794 | | 0.4142 |
| | $j = 4$ | | 0.2330 | | 0.6917 |
| | $j = 5$ | | 0.2134 | | 0.8328 |
| $\ell = 4$ | $j = 3$ | | 0.1140 | | 0.2211 |
| | $j = 4$ | | 0.0622 | | 0.1053 |
| | $j = 5$ | | 0.0485 | | 0.2526 |
| Discretization | | SVI | | ICI | |
| | | Procs | CPU time | Procs | CPU time |
| $\ell = 3$ | $j = 3$ | 512 | 11:43 | 512 | 10:11 |
| | $j = 4$ | 512 | 22:02 | 512 | 16:13 |
| | $j = 5$ | 512 | 42:07 | 512 | 30:36 |
| $\ell = 4$ | $j = 3$ | 1024 | 1:06:44 | 1024 | 56:10 |
| | $j = 4$ | 1024 | 2:06:18 | 1024 | 1:34:51 |
| | $j = 5$ | 1024 | 3:39:28 | 1024 | 2:50:35 |

$$c_{\text{vel}}(v, \mathbf{x}, \mathbf{y}) = \frac{\|\mathbf{x} - \mathbf{y}\|}{|t_{\text{act}}(v, \mathbf{x}) - t_{\text{act}}(v, \mathbf{y})|} \quad \text{with } \bar{\Omega}_{\text{act}}(v) = \{\mathbf{x} \in \Omega : v(t, \mathbf{z}) \geq v_{\text{act}} \text{ for some } t \in [0, T]\} \subset \bar{\Omega} \quad (19)$$

depending on the activation time t_{act}

$$t_{\text{act}}(v, \mathbf{z}) = \min \{t \in [0, T] : v(t, \mathbf{z}) \geq v_{\text{act}}\}, \quad \mathbf{z} \in \bar{\Omega}_{\text{act}} \quad (20)$$

indicating for a point \mathbf{z} the time $t \in [0, T]$ when the transmembrane voltage v is larger than $v_{\text{act}} > v_0$ for the first time. We use $v_{\text{act}} = -40$ mV (see Refs. 8,10) and a spatially constant initial voltage $v_0(\mathbf{x}) = v_0 = -84.57$ mV.

Figure 3 shows the activation patterns in the truncated ellipsoid for two different mesh resolutions. To measure the distance between the two points in the definition of (19), we use the geodesic distance in the truncated ellipsoid. To investigate the space convergence of the CV, we choose two pairs of points $\mathbf{x}, \mathbf{y} \in \bar{\Omega}$: one pair in the center of the myocardial wall and one on the inner surface (details in Table B1). Fixing the step-size at $j = 4$, the conduction velocity converges linearly in space in the center of the myocardial wall and nearly linear at the inner surface points, compare, Table 6.

We observe, that the CV does not change significantly for space discretizations larger than $\ell = 3$. Again, the activation pattern confirms the convergence of the scheme and shows smaller activation times t_{act} for the finer space discretizations.

4.5 | Comparison of the time integration approaches for the transmembrane voltage

Next, we compare the performance of the different splitting approaches defined in Section 3.2. Recall that the gating variables and the calcium concentrations are approximated in exactly the same way in all methods, whereas different approaches are used for the approximation of the transmembrane voltage: the Godunov splitting GS scheme, which is used in most applications, and the three implicit schemes IE-SVI, LI-SVI, and SI-SVI. For the evaluation, we compare the parallel computing time to solve the benchmark problem and the estimated error with respect to the reference solution v_{SI}^{ref}

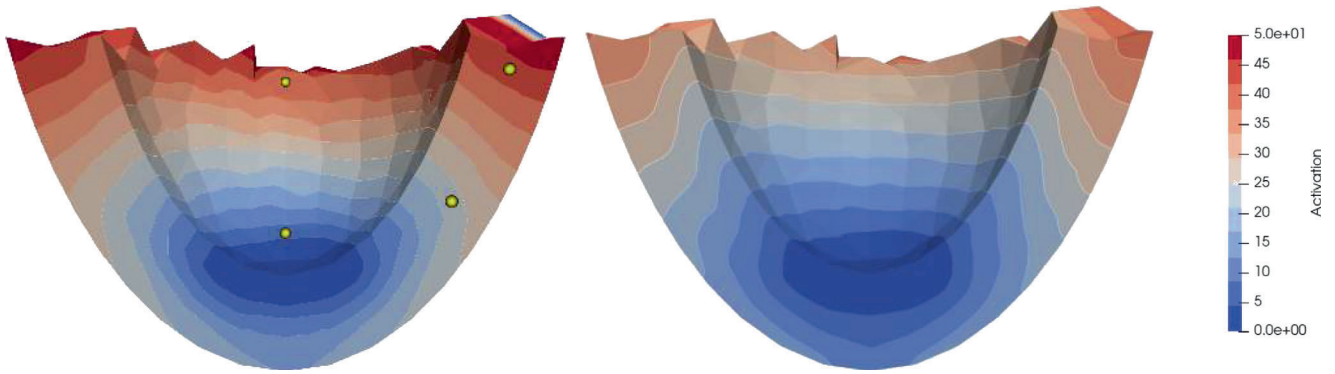


FIGURE 3 Activation pattern for $\ell = 0$ (left, including the evaluation points, compare, Table B1) and for $\ell = 3$ (right, both computed with fixed time level $j = 4$).

TABLE 6 Conduction velocities in m/s computed with the semi-implicit (SI-SVI) scheme on the truncated ellipsoidal mesh (left) and the convergence of the conduction velocities in space (right) both for fixed time $j = 4$.

| | $\mathbf{c}_{\text{vel}}(\mathbf{v}^{j,\ell}, \mathbf{x}_k, \mathbf{y}_k) - \mathbf{c}_{\text{vel}}(\mathbf{v}^{j,\ell-1}, \mathbf{x}_k, \mathbf{y}_k)$ | $\ell = 1$ | $\ell = 2$ | $\ell = 3$ | $\ell = 4$ |
|-----------------------------|---|------------|------------|------------|------------|
| myocardial wall ($k = 1$) | | 0.0530 | 0.0311 | 0.0165 | 0.0068 |
| inner surface ($k = 2$) | | 0.0355 | 0.0242 | 0.0144 | 0.0063 |

$$\eta_{\text{SI}}(\mathbf{z}_k) = \frac{\| \mathbf{v}^{j,\ell}(\cdot, \mathbf{z}_k) - \mathbf{v}_{\text{SI}}^{\text{ref}}(\cdot, \mathbf{z}_k) \|_{L_2(0, T)}}{\| \mathbf{v}_{\text{SI}}^{\text{ref}}(\cdot, \mathbf{z}_k) \|_{L_2(0, T)}}. \quad (21)$$

Figure 4 shows the relation between $\eta_{\text{SI}}(\mathbf{z}_6)$ and CPU time. The number of parallel processes differs for the experiments; thus, to compare the CPU times in Figure 4, they are scaled to 256 processes by multiplying the CPU time with $\#used\ procs/256$.

For a fixed step-size with $j = 4$ (cf. left panel of Figure 4), we observe that SI-SVI is the most efficient scheme, followed by LI-SVI. The accuracy of the implicit Euler method IE-SVI and the linearly implicit scheme LI-SVI are identical, because in our numerical tests it turned out that for the implicit Euler method one single Newton step was sufficient to fulfill the stopping criterion. In this case, IE-SVI and LI-SVI yield exactly the same approximation. The reason why the run-time of IE-SVI is slightly longer is that for the LI-SVI scheme a more efficient assembling routine is realized: the semi-implicit part $B_h^{\Delta t} = C_m M_h + \Delta t A_h$ of the linearization is assembled only once, and in every time step only the nonlinear part of the linearization $\Delta t \partial_v F(t_n, v_h^{n-1}, c_h^n, \mathbf{w}_h^n)$ is computed in addition. This is considerably faster than assembling the full linearization in every Newton step.

For the fixed mesh level $\ell = 4$ (cf. right panel of Figure 4), we also observe that SI-SVI is the most efficient scheme. For the test point \mathbf{z}_6 , the error $\eta_{\text{SI}}(\mathbf{z}_6)$ with respect to the reference solution is not improving for finer time steps with $j > 2$, which indicates that the error of the space discretization dominates. The computing time of the Godunov splitting GS scheme is nearly the same as for the SI-SVI scheme, but the accuracy is considerably worse. The numerical realization of the additional splitting (21) in GS is simpler than the assembling of the right-hand side SI-SVI. On the other hand, the error is larger, for example, the error of $v_{\text{SI-SVI}}^{4,4}$ is smaller than the error of $v_{\text{GS}}^{4,5}$ on the next finer mesh level. The main difference of the schemes is the approximation of the total ionic current as explained in Section 3.2. In summary, for our benchmark scenario the semi-implicit method SI-SVI is the most efficient scheme.

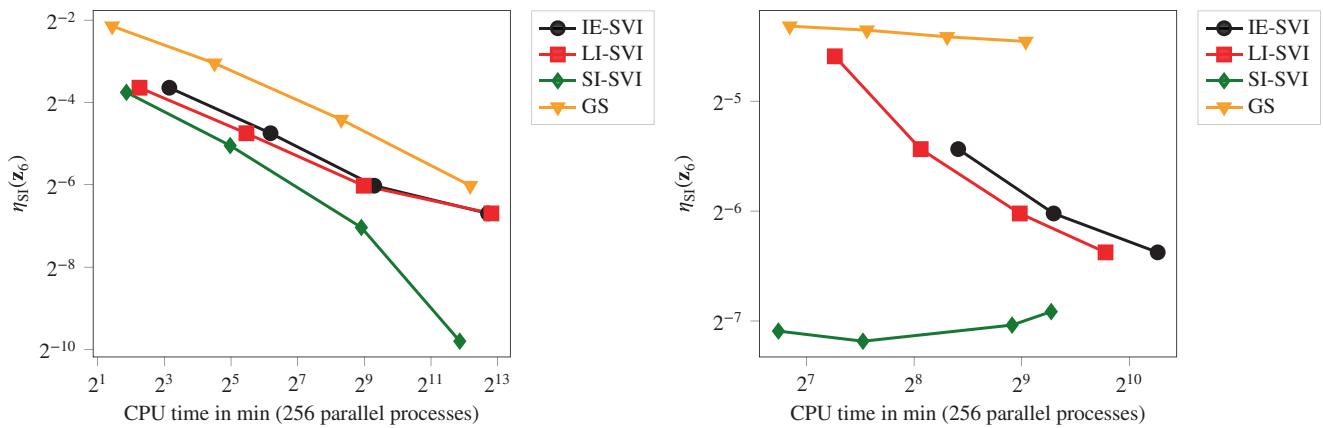


FIGURE 4 Work-precision diagram comparing the different time stepping schemes with fixed time step size with $j = 4$ for mesh levels $\ell \in \{2, 3, 4, 5\}$ (left) and with fixed mesh $\ell = 4$ for $j \in \{2, 3, 4, 5\}$ (right), where the work load is the required CPU time to solve the benchmark problem, and where the precision is estimated by $\eta_{\text{SI}}(\mathbf{z}_6)$.



FIGURE 5 Geometry and coarse mesh on level $\ell = 0$ for the ventricles (left and middle), activation areas $\Omega_{\text{stim},i}$ and starting times $t_{\text{beg},i}$, $i = 1, \dots, 669$ modeling the His-Purkinje system (right). The mesh features holes in the right ventricular outflow tract where the pulmonary artery connects (left) and at the atrio-ventricular valves (middle and right). The entire domain is electrically active.

4.6 | Accuracy of the activation time on a bi-ventricular domain

For the truncated ellipsoid, we observe that SI-SVI is the most efficient scheme. Now we show that this transfers to a full bi-ventricular configuration, compare, Figure 5. The geometric model used in this study is based on magnetic resonance imaging (MRI) data of a 32-year-old healthy volunteer. The interested reader is referred to reference 18 for a detailed description of the model. Here, we use only the ventricular part of the publicly available mesh.²⁶

The convergence is tested by the convergence of the activation times $t_{\text{act}}(v, \mathbf{x})$ at all nodal points $\mathbf{x} \in \mathcal{N}_{h_0}$. This is evaluated for a physiological stimulation scenario at the Purkinje muscle junctions in the ventricles.

The computational domain Ω includes both ventricles. The fiber orientation is defined by a rule-based method^{27,28} with angles ranging from -41° at the epicardium to $+66^\circ$ at the endocardium in agreement with human data from diffusion tensor magnetic resonance imaging.²⁹ The complex stimulation of the ventricles via the His-Purkinje system is represented by the Purkinje muscle junction model as described in reference 30, Chapter 5.3). Every stimulation area $\Omega_{\text{stim},i}$, $i = 1, \dots, 669$, models a leaf of the Purkinje tree, that is, a Purkinje muscle junction, defining $t_{\text{beg},i} \in [0.0, 0.027]$ in seconds while the amplitude $a = 30\text{mV}$ and the duration $\tau = 0.003\text{ s}$ are fixed for all i . For the following numerical experiments, we use the smooth version of the external current I_{ext} in space and time as described in Section 4.1. We set $T = 0.16\text{ s}$, so that in our model the full domain is activated, that is, $\bar{\Omega} = \bar{\Omega}_{\text{act}}$. The discretization data in space are given in Table 7, and in time we use $\Delta t_j = 2^{-j} \Delta t_0$ with $\Delta t_0 = 0.4\text{ms}$. The distribution of the edge length Δx is displayed for the bi-ventricular mesh at $\ell = 0$.

TABLE 7 Mesh data for the space levels ℓ for the bi-ventricular domain and time discretization on time levels j . Here Δx is the length between two nodes of the mesh, the length scale is mm. The edge length and relative frequency for the mesh is shown for $\ell = 0$ (for the refined meshes the edge length and relative frequency is nearly identical).

| ℓ | $\min \Delta x$ | $\max \Delta x$ | # cells | j | N_j | Δt_j (ms) |
|--------|-----------------|-----------------|-----------|-----|-------|-------------------|
| 0 | 0.365865 | 6.189215 | 102625 | 0 | 400 | 0.400 |
| 1 | 0.182933 | 3.216390 | 821000 | 1 | 800 | 0.200 |
| 2 | 0.091466 | 1.608195 | 6568000 | 2 | 1600 | 0.100 |
| 3 | 0.045733 | 0.804098 | 52544000 | 3 | 3200 | 0.050 |
| 4 | 0.022867 | 0.402049 | 420352000 | 4 | 6400 | 0.025 |

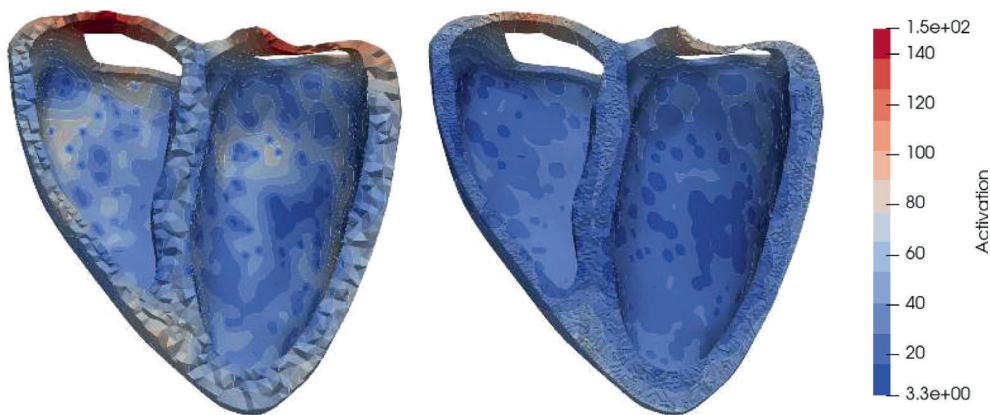
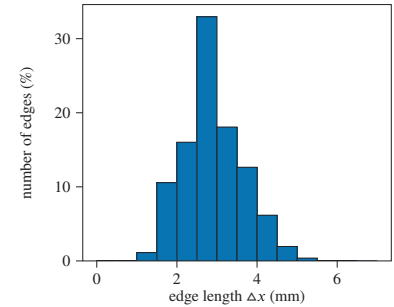


FIGURE 6 Activation pattern for the ventricles with fixed $j = 4$ with $\Delta t_j = 0.00625$ ms for $\ell = 0$ (left) and $\ell = 2$ (right).

For fixed $j = 4$, the distribution of the activation time $t_{\text{act}}(\mathbf{x}, v^{j,\ell})$, $\mathbf{x} \in \bar{\Omega}$, is displayed in Figure 6 for $\ell = 0$ and $\ell = 2$. We observe that the depolarization wave propagates faster on the finer discretization so that the points $\mathbf{x} \in \bar{\Omega} \setminus \Omega_{\text{exc}}$ are earlier activated. As expected, $\ell = 0$ is not fine enough to reproduce the activation time (and thus also the conduction velocity) sufficiently accurate, and for $\ell = 0$ and $j = 0$ the domain is not fully activated (n.f.a.) in $(0, T)$.

To investigate the accuracy and convergence of the activation pattern, we compute

$$t_{\text{act}}(v) = \sqrt{\frac{1}{|\mathcal{N}_{h_0}|} \sum_{\mathbf{x} \in \mathcal{N}_{h_0}} t_{\text{act}}(v, \mathbf{x})^2}, \quad \eta(v, w) = \sqrt{\frac{1}{|\mathcal{N}_{h_0}|} \sum_{\mathbf{x} \in \mathcal{N}_{h_0}} (t_{\text{act}}(v, \mathbf{x}) - t_{\text{act}}(w, \mathbf{x}))^2} \quad (22)$$

for different discretizations, compare, Table 8. We observe in the limit at least linear convergence in space, and the results show clearly that the error in space is dominant, so that in time the resolution for $j = 2$ is sufficient. With larger time steps the activation pattern prescribed by I_{ext} cannot be resolved, so that a minimal resolution of $\Delta t_0 = 0.4$ ms is required. By extrapolation, we can estimate that for the reference solution $v^{4,4}$ the error of $t_{\text{act}}(v^{4,4})$ is below 1%.

The reference solution $v^{4,4}$ is computed on 4096 processor kernels in 5:18 h.

4.7 | A case study with heterogeneous conductivity

Finally we show that our method yields reliable results also in scenarios with spatially heterogeneous conductivity. As an example, we study the case that the conductivity tensor \mathbf{D} is scaled by a factor $1/9$ within a ball of 20 mm radius

TABLE 8 The activation time $t_{\text{act}}(\nu)$ and the difference with respect to the reference solution on different levels in space and time for the semi-implicit (SI-SVI) scheme (the numbers are displayed in ms).

| $t_{\text{act}}(\nu^{j,\ell})$ | $\ell = 0$ | $\ell = 1$ | $\ell = 2$ | $\ell = 3$ | $\ell = 4$ | $\eta(\nu^{j,\ell}, \nu^{4,4})$ | $\ell = 0$ | $\ell = 1$ | $\ell = 2$ | $\ell = 3$ | $\ell = 4$ |
|--------------------------------|------------|------------|------------|------------|------------|---------------------------------|------------|------------|------------|------------|------------|
| $j = 0$ | n.f.a. | 49.7496 | 44.9529 | 43.3617 | 43.3617 | $j = 0$ | n.f.a. | 15.5868 | 10.3322 | 8.6813 | 7.8711 |
| $j = 1$ | 59.2959 | 45.4682 | 40.8133 | 38.8074 | 38.8074 | $j = 1$ | 26.0574 | 11.0463 | 6.0381 | 3.9387 | 2.8940 |
| $j = 2$ | 57.9607 | 43.7983 | 39.0987 | 36.9119 | 36.9119 | $j = 2$ | 24.7093 | 9.2823 | 4.2585 | 1.9524 | 0.8151 |
| $j = 3$ | 57.5546 | 43.2880 | 38.5549 | 36.3082 | 36.3082 | $j = 3$ | 24.2993 | 8.7418 | 3.6952 | 1.3206 | 0.1650 |
| $j = 4$ | 57.4689 | 43.1637 | 38.4167 | 36.1513 | 36.1513 | $j = 4$ | 24.2118 | 8.6060 | 3.5522 | 1.1572 | - |

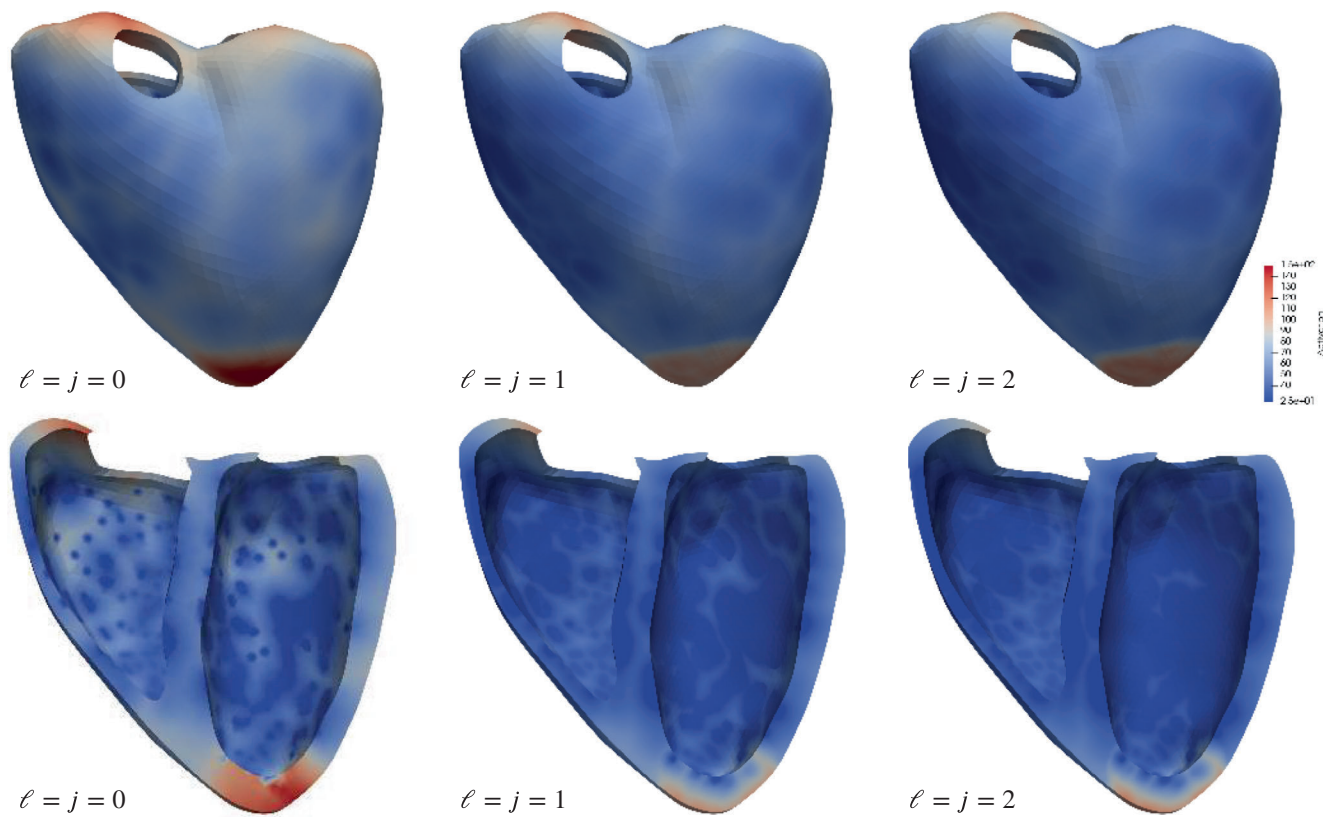


FIGURE 7 Activation time pattern (in ms) in the ventricles for a pathological case with reduced conductivity at the apex.

around the apex, which reduces the conduction velocity approximately by a factor 3. This scenario can be considered as a simplistic representation of a slow conducting myocardial infarction scar. In this case, we observe that the activation time pattern near the apex is qualitatively very well identified already for the coarsest levels in space and time (Figure 7). This coarsest representation can be computed within less than 1 min on node with 64 parallel cores. On levels $\ell = j = 1$ and $\ell = j = 2$ (computed within 1 h on 64 cores), the results on the surface are already quite close. From the convergence test for homogeneous conductivity, we expect also for this application that the overall error is in the range of a few percent.

5 | CONCLUSION

Splitting (and other) methods for advection–diffusion–reaction equations are widely used and have been reviewed in reference 31. A mathematically rigorous error analysis of different splitting methods for various types of nonlinear parabolic PDEs can be found, for example, in references 32–39. A corresponding analysis for the setting considered in this work has, to the best of our knowledge, not been carried out so far.

In this study, we defined a benchmark problem on a truncated ellipsoid approximating the left ventricle. This extends the convergence tests for the conduction velocity in Woodworth et al.¹⁰ for a rectangular domain to unstructured 3d meshes. Moreover, it also extends the results of Pathmanathan et al.¹⁹ to the truncated ellipsoid with the linearly implicit scheme instead of the semi-implicit component-wise splitting scheme and shows that the SVI approach is more efficient than the Lagrange interpolation of the total ionic current ICI. Additionally, we compared the convergence behavior, the accuracy, and the efficiency of different time splitting schemes evaluating the transmembrane voltage. Krishnamoorthi et al. evaluated different lumping variants and the effect of the mesh size on physiological properties such as the conduction velocity of the depolarization wave.¹¹ We confirmed the difference of the approximations by ICI and SVI on the anatomically relevant electrophysiology benchmark problem, and we extended the investigation to a full time and space convergence study. We showed that the reaction–diffusion splitting has the same numerical behavior as the ICI ansatz as it was supposed in reference 19. Furthermore, we showed that a component-wise splitting method with SVI is more

efficient than the reaction–diffusion splitting or component-wise splitting combined with ICI. A main observation is that the stability of component-wise splitting is considerably improved by replacing the Lagrange interpolation in the PDE-ODE coupling by the L_2 projection. The smoothness of the external current in space and time has a strong influence on the convergence properties for solutions of the transmembrane voltage, thus the stimulus current requires suitable regularization. The depolarization changes the transmembrane voltage from approximately -90 to 20 mV within milliseconds, so that time step-sizes $\Delta t < 0.1$ ms are required to capture the fast dynamics. Thus, the time step is so small within the implicit Euler scheme IE-SVI that one Newton step is sufficient to achieve convergence, that is, the linearly implicit method LI-SVI and IE-SVI compute the same approximations. Additionally, we observed that an explicit evaluation of the total ionic current in the semi-implicit scheme SI-SVI does neither deteriorate the accuracy nor causes stability problems although the convergence region is shifted to smaller step-sizes.

The main difference of the Godunov splitting GS and the semi-implicit scheme is the approximation of the total ionic current I_{ion} in space, so that the better performance of SI is mainly due to the better approximation of I_{ion} .

In space, we used linear conforming approximations, which is the standard approach. Nevertheless, a multitude of space discretizations has been studied, for example higher order elements,^{40,41} isoparametric finite elements,^{11,42} adaptive methods^{43,44} and non-conforming elements.⁴⁵ Our results complement these contributions by a comparison of time discretizations. For the monodomain system, also further finite methods including discontinuous Galerkin approximations were proposed.^{44,46} since our finite element system M++ also includes nonconforming and discontinuous Galerkin approximations, future studies will investigate the synergy between modern discretization in space and optimal time stepping.

For this study, we restricted ourselves to the monodomain equation coupled with the Beeler–Reuter cell model¹⁷ describing the evolution of the calcium ion concentration and six gating variables. This cell model is well established and includes the characteristic properties (including fast gating kinetics) which make the design of efficient and stable schemes challenging. The advantages of SI-SVI or LI-SVI will likely transfer to more complex cell models, as the model by ten Tusscher and Panfilov,⁴⁷ O'Hara and Rudy⁴⁸ or Courtemanche.⁴⁹

The results from the benchmark problem were extended to a realistic bi-ventricular setting, where we investigated the convergence in space and time as well as the accuracy of the activation times using the semi-implicit scheme proposed in reference 14. We showed that the results for the benchmark problem of the truncated ellipsoid transfer to an anatomically even more realistic setup of a bi-ventricular mesh with a complex stimulation model by a convergence study for the activation time. The activation pattern converges at least linear in space using the SI-SVI and the dominance of the space error on the coarse meshes is confirmed. In particular, we demonstrated that state-of-the-art high-performance computing facilities and the efficient realization of parallel numerical methods can approximate complex models very accurately within reasonable computing time.

We showed that using the semi-implicit SI-SVI or the linearly implicit LI-SVI scheme will increase stability and accuracy on irregular complex coarse meshes. The proposed time integration schemes can be adapted by established cardiac electrophysiology simulation packages,²² can be incorporated in full heart electro-mechanical simulations¹⁸ and potentially also in other application domains like modeling of gastrointestinal electrophysiology.⁵⁰

ACKNOWLEDGMENT

Funded by the Deutsche Forschungsgemeinschaft (DFG, German Research Foundation), Project-ID 258734477, SFB 1173 and Project-ID 465189069, SPP 2311. This work was performed on the HoreKa supercomputer funded by the Ministry of Science, Research and the Arts Baden-Württemberg and by the Federal Ministry of Education and Research. Open Access funding enabled and organized by Projekt DEAL.

CONFLICT OF INTEREST

The authors declare no potential conflict of interests.

DATA AVAILABILITY STATEMENT

The data that support the findings of this study are openly available in mpp/cardmech/-/tree/1.0.3 at <https://git.scc.kit.edu>.

ORCID

Tobias Jahnke  <https://orcid.org/0000-0003-4480-8055>

Axel Loewe  <https://orcid.org/0000-0002-2487-4744>

Christian Wieners  <https://orcid.org/0000-0001-6242-6777>

REFERENCES

1. Franzone PC, Savaré G. Degenerate evolution systems modeling the cardiac electric field at micro- and macroscopic level. In: Lorenz A, Ruf B, eds. *Evolution Equations, Semigroups and Functional Analysis. Progress in Nonlinear Differential Equations and their Applications*. Birkhäuser; 2002:49-78.
2. Bourgault Y, Pierre C. Comparing the Bidomain and Monodomain Models in Electro-Cardiology through Convergence Analysis; 2010. <https://hal.archives-ouvertes.fr/hal-00545888v2>.
3. Sundnes J, Lines GT, Tveito A. An operator splitting method for solving the bidomain equations coupled to a volume conductor model for the torso. *Math Biosci*. 2005;194(2):233-248.
4. Qu Z, Garfinkel A. An advanced algorithm for solving partial differential equation in cardiac conduction. *IEEE Trans Biomed Eng*. 1999; 46(9):1166-1168.
5. Rush S, Larsen H. A practical algorithm for solving dynamic membrane equations. *IEEE Trans Biomed Eng*. 1978;4:389-392.
6. Niederer SA, Kerfoot E, Benson AP, et al. Verification of cardiac tissue electrophysiology simulators using an N-version benchmark. *Philos Trans R Soc A Math Phys Eng Sci*. 1954;2011(369):4331-4351.
7. Pezzuto S, Hake J, Sundnes J. Space-discretization error analysis and stabilization schemes for conduction velocity in cardiac electrophysiology. *Int J Numer Methods Biomed Eng*. 2016;32(10):e02762.
8. Woodworth LA, Cansz B, Kaliske M. Balancing conduction velocity error in cardiac electrophysiology using a modified quadrature approach. *Int J Numer Methods Biomed Eng*. 2022;36(5):e3589.
9. Roy T, Bourgault Y, Pierre C. Analysis of time-stepping methods for the monodomain model. *Comput Appl Math*. 2020;39(3):1-32.
10. Woodworth LA, Cansz B, Kaliske M. A numerical study on the effects of spatial and temporal discretization in cardiac electrophysiology. *Int J Numer Methods Biomed Eng*. 2021;37(5):e3443. doi:10.1002/cnm.3443
11. Krishnamoorthi S, Sarkar M, Klug WS. Numerical quadrature and operator splitting in finite element methods for cardiac electrophysiology. *Int J Numer Methods Biomed Eng*. 2013;29(11):1243-1266.
12. Land S, Gurev V, Arens S, et al. Verification of cardiac mechanics software: benchmark problems and solutions for testing active and passive material behaviour. *Proc R Soc Lond A*. 2015;471(2184):20150641. doi:10.1098/rspa.2015.0641
13. Bendahmane M, Mroue F, Saad M. A positive cell vertex Godunov scheme for a Beeler-Reuter based model of cardiac electrical activity. *Numer Methods Partial Diff Equat*. 2021;37(1):262-301.
14. Caligari S, Scacchi S. Mathematical and numerical modeling of reentrant ventricular arrhythmias in the presence of Brugada syndrome. *Annals Alexandru Ioan Cuza University-Mathematics*. 2020;66(2):301-322.
15. Baumgarten N, Wieners C. The parallel finite element system M++ with integrated multilevel preconditioning and multilevel Monte Carlo methods. *Comput Math Appl*. 2021;81:391-406. doi:10.1016/j.camwa.2020.03.004
16. Vigmond E, Dos Santos RW, Prassl A, Deo M, Plank G. Solvers for the cardiac bidomain equations. *Prog Biophys Mol Biol*. 2008;96(1-3): 3-18.
17. Beeler GW, Reuter H. Reconstruction of the action potential of ventricular myocardial fibres. *J Physiol*. 1977;268(1):177-210.
18. Gerach T, Schuler S, Fröhlich J, et al. Electro-mechanical whole-heart digital twins: a fully coupled multi-physics approach. *Mathematics*. 2021;9(11):1247. doi:10.3390/math9111247
19. Pathmanathan P, Mirams GR, Southern J, Whiteley JP. The significant effect of the choice of ionic current integration method in cardiac electro-physiological simulations. *Int J Numer Methods Biomed Eng*. 2011;27(11):1751-1770.
20. Marsh ME, Ziaratgahi ST, Spiteri RJ. The secrets to the success of the Rush-Larsen method and its generalizations. *IEEE Transact Biomed Eng*. 2012;59(9):2506-2515.
21. Sundnes J, Artebrant R, Skavhaug O, Tveito A. A second-order algorithm for solving dynamic cell membrane equations. *IEEE Trans Biomed Eng*. 2009;56(10):2546-2548.
22. Plank G, Loewe A, Neic A, et al. The openCARP simulation environment for cardiac electrophysiology. *Comput Methods Programs Biomed*. 2021;208:106223. doi:10.1016/j.cmpb.2021.106223
23. Lindner L. CardMech framework of M++. <https://git.scc.kit.edu/mpp/cardmech/-/tree/1.0.2>.
24. Coudière Y, Douanla Lonsi C, Pierre C. Rush-Larsen time-stepping methods of high order for stiff problems in cardiac electrophysiology. *Electron Trans Numer Anal*. 2020;52:342-357. doi:10.1553/etna_vol52s342
25. Gander W, Gander MJ, Kwok F. *Scientific Computing – an Introduction Using Maple and MATLAB*. Vol 11. Springer Science & Business; 2014.
26. Gerach T, Schuler S, Wachter A, Loewe A. Four-chamber human heart model for the simulation of cardiac electrophysiology and cardiac mechanics. *Zenodo*. 2021. doi:10.5281/zenodo.5573921
27. Bayer JD, Blake RC, Plank G, Trayanova NA. A novel rule-based algorithm for assigning myocardial fiber orientation to computational heart models. *Ann Biomed Eng*. 2012;40(10):2243-2254.
28. Schuler S. KIT-IBT/LDRB_Fibers. 2021. doi: 10.5281/zenodo.4606575
29. Lombaert H, Peyrat JM, Croisille P, et al. Human atlas of the cardiac fiber architecture: study on a healthy population. *IEEE Trans Med Imaging*. 2012;31(7):1436-1447. doi:10.1109/TMI.2012.2192743
30. Gerach T. Personalized Electromechanical Modeling of the Human Heart: Challenges and Opportunities for the Simulation of Pathophysiological Scenarios 2022. doi: 10.5445/IR/1000147806
31. Hundsdorfer W, Verwer J. Numerical solution of time-dependent advection-diffusion-reaction equations. *33 of Springer Series in Computational Mathematics*. Springer-Verlag; 2003.

32. Hansen E, Ostermann A. Dimension splitting for quasilinear parabolic equations. *IMA J Numer Anal.* 2010;30(3):857-869. doi:[10.1093/imanum/drn078](https://doi.org/10.1093/imanum/drn078)
33. Hansen E, Ostermann A. High-order splitting schemes for semilinear evolution equations. *BIT.* 2016;56(4):1303-1316. doi:[10.1007/s10543-016-0604-2](https://doi.org/10.1007/s10543-016-0604-2)
34. Einkemmer L, Ostermann A. Overcoming order reduction in diffusion-reaction splitting. Part 2: oblique boundary conditions. *SIAM J Sci Comput.* 2016;38(6):A3741-A3757. doi:[10.1137/16M1056250](https://doi.org/10.1137/16M1056250)
35. Descombes S. Convergence of a splitting method of high order for reaction-diffusion systems. *Math Comput.* 2001;70(236):1481-1501. doi:[10.1090/S0025-5718-00-01277-1](https://doi.org/10.1090/S0025-5718-00-01277-1)
36. Altmann R, Ostermann A. Splitting methods for constrained diffusion-reaction systems. *Comput Math Appl.* 2017;74(5):962-976. doi:[10.1016/j.camwa.2017.02.044](https://doi.org/10.1016/j.camwa.2017.02.044)
37. Karlsen KH, Risebro NH. Corrected operator splitting for nonlinear parabolic equations. *SIAM J Numer Anal.* 2000;37(3):980-1003. doi:[10.1137/S0036142997320978](https://doi.org/10.1137/S0036142997320978)
38. Descombes S, Ribot M. Convergence of the Peaceman-Rachford approximation for reaction-diffusion systems. *Numer Math.* 2003;95(3):503-525. doi:[10.1007/s00211-002-0434-9](https://doi.org/10.1007/s00211-002-0434-9)
39. Hansen E, Henningsson E. A convergence analysis of the Peaceman-Rachford scheme for semilinear evolution equations. *SIAM J Numer Anal.* 2013;51(4):1900-1910. doi:[10.1137/120890570](https://doi.org/10.1137/120890570)
40. Arthurs CJ, Bishop MJ, Kay D. Efficient simulation of cardiac electrical propagation using high order finite elements. *J Comput Phys.* 2012;231(10):3946-3962.
41. Vincent KP, Gonzales MJ, Gillette AK, et al. High-order finite element methods for cardiac monodomain simulations. *Front Physiol.* 2015;6:217. doi:[10.3389/fphys.2015.00217](https://doi.org/10.3389/fphys.2015.00217)
42. Patelli AS, Dedè L, Lassila T, Bartezzaghi A, Quarteroni A. Isogeometric approximation of cardiac electrophysiology models on surfaces: an accuracy study with application to the human left atrium. *Comput Methods Appl Mech Eng.* 2017;317:248-273.
43. Heidenreich EA, Ferrero JM, Doblaré M, Rodríguez JF. Adaptive macro finite elements for the numerical solution of monodomain equations in cardiac electrophysiology. *Ann Biomed Eng.* 2010;38(7):2331-2345.
44. Hoermann JM, Bertoglio C, Kronbichler M, Pfaller MR, Chabiniok R, Wall WA. An adaptive hybridizable discontinuous Galerkin approach for cardiac electrophysiology. *Int J Numer Methods Biomed Eng.* 2018;34(5):e2959.
45. Hurtado DE, Rojas G. Non-conforming finite-element formulation for cardiac electrophysiology: an effective approach to reduce the computation time of heart simulations without compromising accuracy. *Comput Mech.* 2018;61(4):485-497.
46. Rocha BM, Dos Santos RW, Igreja I, Loula AF. Stabilized hybrid discontinuous Galerkin finite element method for the cardiac monodomain equation. *Int J Numer Methods Biomed Eng.* 2020;36(7):e3341.
47. ten Tusscher KH, Panfilov AV. Alternans and spiral breakup in a human ventricular tissue model. *Am J Phys Heart Circ Phys.* 2006;291(3):H1088-H1100. doi:[10.1152/ajpheart.00109.2006](https://doi.org/10.1152/ajpheart.00109.2006)
48. O'Hara T, Virág L, Varró A, Rudy Y. Simulation of the undiseased human cardiac ventricular action potential: model formulation and experimental validation. *PLoS Comput Biol.* 2011;7(5):e1002061.
49. Courtemanche M, Ramirez RJ, Nattel S. Ionic mechanisms underlying human atrial action potential properties: insights from a mathematical model. *Am J Phys Heart Circ Phys.* 1998;275(1):H301-H321.
50. Du P, O'Grady G, Davidson JB, Cheng LK, Pullan AJ. Multiscale modeling of gastrointestinal electrophysiology and experimental validation. *Crit Rev Biomed Eng.* 2010;38(3):225-254. doi:[10.1615/critrevbiomedeng.v38.i3.10](https://doi.org/10.1615/critrevbiomedeng.v38.i3.10)

How to cite this article: Lindner LP, Gerach T, Jahnke T, Loewe A, Weiss D, Wieners C. Efficient time splitting schemes for the monodomain equation in cardiac electrophysiology. *Int J Numer Meth Biomed Engng.* 2023; e3666. doi:[10.1002/cnm.3666](https://doi.org/10.1002/cnm.3666)

APPENDIX A: The Beeler–Reuter cell model

The Beeler–Reuter cell model¹⁷ is defined by the transmembrane voltage v , the intracellular ion concentration of calcium c , and six gating mechanisms $\mathbf{w} = (w_1, \dots, w_6) = (d, f, m, h, j, x_1)$. The total ionic current $I_{\text{ion}}(v, c, \mathbf{w})$ is the sum of the two inward currents

$$I_s(v, c, d, f) = g_s df(v - E_s(c)), \quad I_{\text{Na}}(v, m, h, j) = (g_{\text{Na}} m^3 h j + g_{\text{NaC}})(v - E_{\text{Na}}),$$

and the two outward currents

$$I_{x_1}(v, x_1) = x_1 \frac{0.8(\exp(0.04(v+77)) - 1)}{\exp(0.04(v+35))}, \quad I_K(v) = \frac{1.4(\exp(0.04(v+85)) - 1)}{\exp(0.08(v+53)) + \exp(0.04(v+53))} + \frac{0.07(v+23)}{1 - \exp(-0.04(v+23))},$$

with the reversal potential $E_s(c) = -82.3 - 13.0287 \log(c)$ and $E_{\text{Na}} = 50$ mV. Corresponding to reference 17 the constants are set to

$$g_{\text{Na}} = 4 \text{ mS/cm}^2, \quad g_{\text{NaC}} = 0.003 \text{ mS/cm}^2, \quad g_s = 0.09 \text{ mS/cm}^2.$$

The opening and closing rates $\alpha_k(v)$ and $\beta_k(v)$ in (5) are defined by

$$\alpha_k(v) = \frac{C_{1,k} \exp(C_{2,k}(v + C_{3,k})) + C_{4,k}(v + C_{5,k})}{\exp(C_{6,k}(v + C_{3,k})) + C_{7,k}}, \quad \beta_k(v) = \frac{C_{1,k} \exp(C_{2,k}(v + C_{3,k})) + C_{4,k}(v + C_{5,k})}{\exp(C_{6,k}(v + C_{3,k})) + C_{7,k}}$$

depending on different parameters $C_{1,k}, \dots, C_{7,k} \geq 0$ for $k = 1, \dots, 6$, compare, Table A1.

The potentials are given in mV, the calcium concentration in mol/l and the gating variables are dimensionless. The initial values at $t = 0$ are constant in space and set to.

$$v^0 = -84.57 \text{ mV}, \quad \text{Ca}^0 = 0.0000002 \frac{\text{mol}}{\text{l}}, \quad \mathbf{w}^0 = (0.002980, 1.0, 0.9877, 0.975, 0.011, 0.00565).$$

In G_c from (6) the constants are defined as $w_c = 0.07$ and $\alpha_c = 10^{-7}$. As the gating variables model the status of a gate they switch very fast between zero and one and adopt only values in $[0, 1]$. As c models the calcium concentration in a

TABLE A1 Constants to define α_y and β_y for every gate with Equation (9).

| | $C_{1,k}$ | $C_{2,k}$ | $C_{3,k}$ | $C_{4,k}$ | $C_{5,k}$ | $C_{6,k}$ | $C_{7,k}$ |
|--------------------------------|-----------------------|-----------------------|-----------|---------------------------------------|-----------|-----------------------|-----------|
| $\alpha_m \equiv \alpha_3$ | 0 | 0 | 47 | -1 | 47 | -0.1 | -1 |
| $\beta_m \equiv \beta_3$ | 40 | -0.056 | 72 | 0 | 0 | 0 | 0 |
| $\alpha_h \equiv \alpha_4$ | 0.126 | -0.25 | 77 | 0 | 0 | 0 | 0 |
| $\beta_h \equiv \beta_4$ | 1.7 | 0 | 22.5 | 0 | 0 | -0.082 | 1 |
| $\alpha_j \equiv \alpha_5$ | 0.055 | -0.25 | 78 | 0 | 0 | -0.2 | 1 |
| $\beta_j \equiv \beta_5$ | 0.3 | 0 | 32 | 0 | 0 | -0.1 | 1 |
| $\alpha_d \equiv \alpha_1$ | 0.095 | -0.01 | -5 | 0 | 0 | -0.072 | 1 |
| $\beta_d \equiv \beta_1$ | 0.07 | -0.017 | 44 | 0 | 0 | 0.05 | 1 |
| $\alpha_f \equiv \alpha_2$ | 0.012 | -0.008 | 28 | 0 | 0 | 0.15 | 1 |
| $\beta_f \equiv \beta_2$ | 0.0065 | -0.02 | 30 | 0 | 0 | -0.2 | 1 |
| $\alpha_{x_1} \equiv \alpha_6$ | 0.0005 | 0.083 | 50 | 0 | 0 | 0.057 | 1 |
| $\beta_{x_1} \equiv \beta_6$ | 0.0013 | -0.06 | 20 | 0 | 0 | -0.04 | 1 |
| $\frac{1}{\text{ms}}$ | $\frac{1}{\text{ms}}$ | $\frac{1}{\text{mV}}$ | mV | $\frac{1}{\text{mV} \cdot \text{ms}}$ | mV | $\frac{1}{\text{mV}}$ | — |

cardiac cell it is always positive and during one action potential it has values between $[2 \cdot 10^{-7}, 6 \cdot 10^{-6}]$ mol/l. The physiological range of the transmembrane voltage v is in $[-90, 20]$ mV.

APPENDIX B: Numerical setup

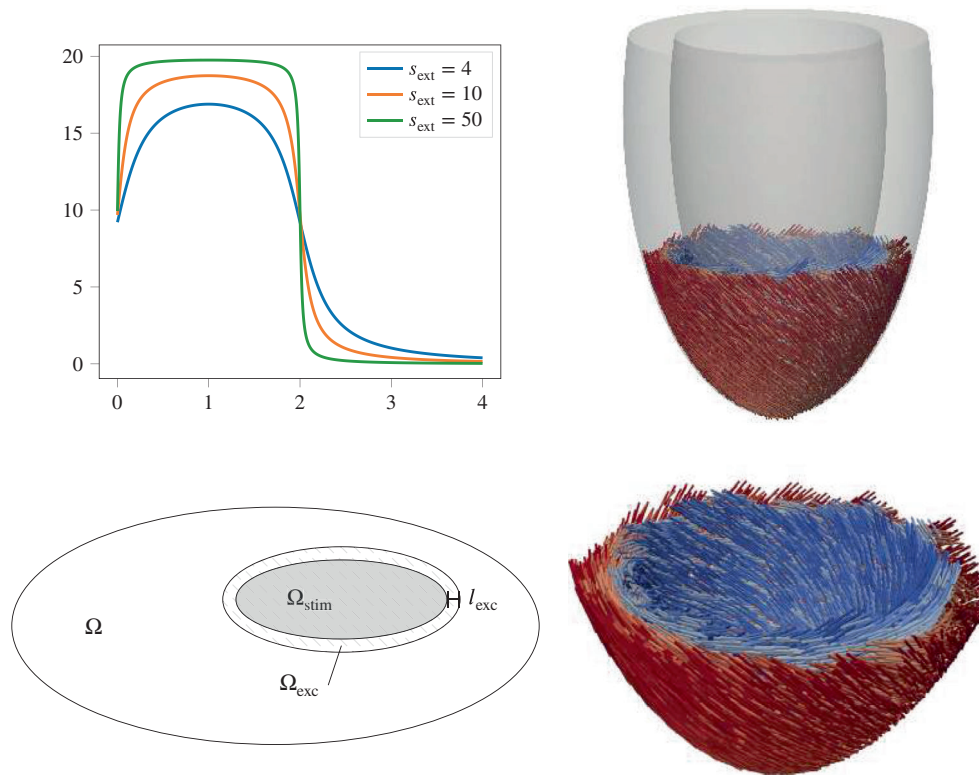


FIGURE B1 Smoothed external stimulus for different s_{ext} with fixed $a = 20$, $t_{beg} = 0$, $\tau = 2$ and example to illustrate $\bar{\Omega}_{exc}$ (left) and visualization of the full ellipsoid and fiber orientation in the truncated ellipsoid (right).

B.1 | Parameters and constants for the numerical simulations

The domain $\bar{\Omega}$ is measured in mm. The surface-to-volume-ratio is given by $\chi = 140 \text{ mm}^{-1}$, the membrane capacitance is set to $C_m = 0.01 \cdot 10^{-6} \text{ F/mm}^2$, and the anisotropic conductivity in (16) is defined by the parameters

TABLE B1 Evaluation points in the truncated ellipsoid, compare, Figures 1 and 3.

| | |
|---|--|
| $\mathbf{z}_1 = (0.0, 0.0, -17.0)$ | Grid point at apex endocardial excited |
| $\mathbf{z}_2 = (0.0, 0.0, -20.0)$ | Grid point at apex epicardial |
| $\mathbf{z}_3 = (0.88, 3.28, -16.95)$ | Grid point inner wall middle of ellipsoid |
| $\mathbf{z}_4 = (0.2, 0.2, -17.4)$ | Besides grid next to \mathbf{z}_1 |
| $\mathbf{z}_5 = (0.1, 0.1, -19.8)$ | Besides grid next to \mathbf{z}_2 |
| $\mathbf{z}_6 = (-0.98, -3.3, -16.2)$ | Besides grid next to \mathbf{z}_3 |
| $\mathbf{z}_7 = (-1.6, 4.5, -15.8)$ | Besides grid in wall, Opposite(y-direction) of \mathbf{z}_6 |
| $\mathbf{x}_1 = (-2.571, 0.0, -15.811)$ $\mathbf{y}_1 = (-5.617, 0.0, -10.105)$ | Myocardial wall |
| $\mathbf{x}_2 = (0.0, 5.166, -14.656)$ $\mathbf{y}_2 = (0.0, 6.971, -10.556)$ | Inner surface |

$$D_1 = 0.0001334177215 \text{ Smm}^{-1}, \quad D_t = 0.00001760617761 \text{ Smm}^{-1}.$$

The mesh data and the fiber orientation are available in the data file `data/monodomain/Orientation.vtu` within our git repository.²³ A standard choice for the constants of the external current is the amplitude $a(\mathbf{x}) = 20 \mu\text{A}/\text{cm}^2$ for all $\mathbf{x} \in \overline{\Omega}_{\text{stim}}$, the scaling factor $s_{\text{ext}} = 4$, the start time $t_{\text{beg},i} = 0.0$ and $\tau_j = 0.002 \text{ s}$ for all $i = 1, \dots, n_{\text{stim}}$. In Figure B1 the dependence of the time-continuous version of I_{ext} on the scaling factor s_{ext} is plotted at one stimulation point for fixed amplitude and duration (Table B1).